Measurement of Atmospheric Neutrino Oscillation Parameters Using Convolutional Neural Networks with 9.3 Years of Data in IceCube DeepCore

R. Abbasi, ¹⁷ M. Ackermann, ⁶⁵ J. Adams, ¹⁸ S. K. Agarwalla, ^{40,*} J. A. Aguilar, ¹² M. Ahlers, ²² J. M. Alameddine, ²³ N. M. Amin, ⁴⁴ K. Andeen, ⁴² G. Anton, ²⁶ C. Argüelles, ¹⁴ Y. Ashida, ⁵³ S. Athanasiadou, ⁶⁵ L. Ausborm, ¹ S. N. Axani, ⁴⁴ X. Bai, ⁵⁰ A. Balagopal V., ⁴⁰ M. Baricevic, ⁴⁰ S. W. Barwick, ³⁰ S. Bash, ²⁷ V. Basu, ⁴⁰ R. Bay, ⁸ J. J. Beatty, ^{20,21} J. Becker Tjus, ^{11,†} J. Beise, ⁶³ C. Bellenghi, ²⁷ C. Benning, ¹ S. BenZvi, ⁵² D. Berley, ¹⁹ E. Bernardini, ⁴⁸ D. Z. Besson, ³⁶ E. Blaufuss, ¹⁹ L. Bloom, ⁶⁰ S. Blot, ⁶⁵ F. Bontempo, ³¹ J. Y. Book Motzkin, ¹⁴ C. Boscolo Meneguolo, ⁴⁸ S. Böser, ⁴¹ O. Botner, ⁶³ J. Böttcher, ¹ E. Bourbeau, ²² J. Braun, ⁴⁰ B. Brinson, ⁶ J. Brostean-Kaiser, ⁶⁵ L. Brusa, ¹ R. T. Burley, ² D. Butterfield, ⁴⁰ M. A. Campana, ⁴⁹ I. Caracas, ⁴¹ K. Carloni, ¹⁴ J. Carpio, ^{34,35} S. Chattopadhyay, ^{40,*} N. Chau, ¹² Z. Chen, ⁵⁶ D. Chirkin, ⁴⁰ S. Choi, ^{57,58} B. A. Clark, ¹⁹ A. Coleman, ⁶³ G. H. Collin, ¹⁵ A. Connolly, ^{20,21} J. M. Conrad, ¹⁵ P. Coppin, ¹³ R. Corley, ⁵³ P. Correa, ¹³ D. F. Cowen, ^{61,62} P. Dave, ⁶ C. De Clercq, ¹³ J. J. DeLaunay, ⁶⁰ D. Delgado, ¹⁴ S. Deng, ¹ A. Desai, ⁴⁰ P. Desiati, ⁴⁰ K. D. de Vries, ¹³ G. de Wasseige, ³⁷ T. DeYoung, ²⁴ A. Diaz, ¹⁵ J. C. Díaz-Vélez, ⁴⁰ P. Dierichs, ¹ M. Dittmer, ⁴³ A. Domi, ²⁶ L. Draper, ⁵³ H. Dujmovic, ⁴⁰ K. Dutta, ⁴¹ M. A. DuVernois, ⁴⁰ T. Ehrhardt, ⁴¹ L. Eidenschink, ²⁷ A. Eimer, ²⁶ P. Eller, ²⁷ E. Ellinger, ⁶⁴ S. El Mentawi, ¹ D. Elsässer, ²³ R. Engel, ^{31,32} H. Erpenbeck, ⁴⁰ J. Evans, ¹⁹ P. A. Evenson, ⁴⁴ K. L. Fan, ¹⁹ K. Fang, ⁴⁰ K. Farrag, ¹⁶ A. R. Fazely, ⁷ A. Fedynitch, ⁵⁹ N. Feigl, ¹⁰ S. Fiedlschuster, ²⁶ C. Finley, ⁵⁵ L. Fischer, ⁶⁵ A. R. Fazely, ⁷ A. Fedynitch, ⁵⁹ N. Feigl, ¹⁰ S. Fiedlschuster, ²⁶ C. Finley, ⁵⁵ L. Fischer, ⁶⁵ A. R. Fazely, ⁷ A. Fedynitch, ⁵⁹ N. Feigl, ¹⁰ S. Fiedlschuster, ²⁶ C. Finley, ⁵⁵ L. Fischer, ⁶⁵ A. R. Fazely, ⁷ A. Fedynitch, ⁵⁹ N. Feigl, ¹⁰ S. Fiedlschuster, ²⁶ C. Finley, ⁵⁵ L. Fischer, ⁶⁵ A. R. Fazely, ⁷ A. Fedynitch, ⁵⁹ N. Feigl, ¹⁰ S. Fiedlschuster, ²⁶ C. Finley, ⁵⁵ L. Fischer, ⁶⁵ A. R. Fazely, ⁷ A. Fedynitch, ⁷⁹ N. Feigl, ¹⁰ S. Fiedlschuster, ²⁶ C. Finley, ⁵⁵ L. Fischer, ⁶⁵ A. R. Fazely, ⁷ A. Fedynitch, ⁷⁹ N. Feigl, ¹⁰ S. Fiedlschuster, ²⁶ C. Finley, ⁵⁵ L. Fischer, ⁶⁵ A. R. Fazely, ⁷ A. Fedynitch, ⁷⁹ N. Feigl, ¹⁰ S. Fiedlschuster, ²⁶ C. Finley, ⁵⁵ L. Fischer, ⁶⁵ A. R. Fazely, ⁷ A. Fedynitch, ⁷⁹ N. Feigl, ⁷⁰ S. Fiedlschuster, ⁷⁰ C. Finley, ⁷⁰ L. Fischer, ⁷⁰ A. Fedynitch, ⁷⁰ R. Fiedlschuster, ⁷⁰ P. A. Fedynitch, ⁷⁰ R. Fedynitch, ⁷⁰ R. Fiedlschuster, ⁷⁰ R. Fiedlschuster, ⁷⁰ R. Fedynitch, D. Fox, 61 A. Franckowiak, 11 S. Fukami, 65 P. Fürst, 1 J. Gallagher, 39 E. Ganster, 1 A. Garcia, 44 G. Garg, 40,* E. Genton, ^{14,37} L. Gerhardt, ⁹ A. Ghadimi, ⁶⁰ C. Girard-Carillo, ⁴¹ C. Glaser, ⁶³ T. Glüsenkamp, ^{26,63} J. G. Gonzalez, ⁴⁴ S. Goswami, ^{34,35} A. Granados, ²⁴ D. Grant, ^{24,¶} S. J. Gray, ¹⁹ O. Gries, ¹ S. Griffin, ⁴⁰ S. Griswold, ⁵² K. M. Groth, ²² C. Günther, ¹ P. Gutjahr, ²³ C. Ha, ⁵⁴ C. Haack, ²⁶ A. Hallgren, ⁶³ L. Halve, ¹ F. Halzen, ⁴⁰ H. Hamdaoui, ⁵⁶ M. Ha Minh, ²⁷ C. Handan, ²⁸ C. Handan, C. Günther, P. Gutjahr, C. Ha, C. Haack, A. Hallgren, L. Halve, F. Halzen, H. Hamdaoui, M. Ha Minh, M. Handt, K. Hanson, J. Hardin, A. A. Harnisch, P. Hatch, A. Haungs, J. Haußler, K. Helbing, L. Hellrung, L. Heuermann, N. Heyer, S. Hickford, A. Hidvegi, J. Hignight, C. Hill, G. C. Hill, K. D. Hoffman, S. Hori, M. Hostert, M. Hostert, W. Hou, T. Huber, K. Hultqvist, M. Hünnefeld, R. Hussain, K. Hultqvist, M. Hignight, M. Hussain, M. Hussain, K. Hultqvist, M. Hünnefeld, M. Jacquart, O. Janik, M. Jansson, M. Jansson, G. S. Japaridze, M. Jeong, M. Jin, H. B. J. P. Jones, N. Kamp, L. Kang, W. Kang, X. Kang, A. Kappes, A. Kappesser, L. Kardum, T. Karg, M. Karl, A. Karle, A. Karle, A. Karle, G. R. Klein, R. A. Kochocki, A. Kochocki, A. Koirala, H. Kolanoski, M. Karle, A. Karle, A. Karle, R. Kolanoski, M. Kaypelski, M. Karle, A. Karle, R. Korrala, A. Kaypelski, M. T. Kontrimas,²⁷ L. Köpke,⁴¹ C. Kopper,²⁶ D. J. Koskinen,²² P. Koundal,⁴⁴ M. Kovacevich,⁴⁹ M. Kowalski,^{10,65} T. Kozynets,²² J. Krishnamoorthi,^{40,*} K. Kruiswijk,³⁷ E. Krupczak,²⁴ A. Kumar,⁶⁵ E. Kun,¹¹ N. Kurahashi,⁴⁹ N. Lad,⁶⁵ C. Lagunas Gualda,⁶⁵ M. Lamoureux,³⁷ M. J. Larson,¹⁹ S. Latseva,¹ F. Lauber,⁶⁴ J. P. Lazar,³⁷ J. W. Lee,⁵⁷ K. Leonard DeHolton, ⁶² A. Leszczyńska, ⁴⁴ J. Liao, ⁶ M. Lincetto, ¹¹ Y. T. Liu, ⁶² M. Liubarska, ²⁵ E. Lohfink, ⁴¹ C. Love, ⁴⁹ C. J. Lozano Mariscal, ⁴³ L. Lu, ⁴⁰ F. Lucarelli, ²⁸ W. Luszczak, ^{20,21} Y. Lyu, ^{8,9} W. Y. Ma, ⁶⁵ J. Madsen, ⁴⁰ E. Magnus, ¹³ K. B. M. Mahn, ²⁴ Y. Makino, ⁴⁰ E. Manao, ²⁷ S. Mancina, ^{40,48} W. Marie Sainte, ⁴⁰ I. C. Mariş, ¹² S. Marka, ⁴⁶ Z. Marka, ⁴⁶ M. Marsee, ⁶⁰ I. Martinez-Soler, ¹⁴ R. Maruyama, ⁴⁵ F. Mayhew, ²⁴ F. McNally, ³⁸ J. V. Mead, ²² K. Meagher, ⁴⁰ S. Mechbal, ⁶⁵ A. Medina, ²¹ M. Meier, ¹⁶ Y. Merckx, ¹³ L. Merten, ¹¹ J. Micallef, ²⁴, § J. Mitchell, ⁷ T. Montaruli, ²⁸ R. W. Moore, ²⁵ Y. Morii, ¹⁶ R. Morse, 40 M. Moulai, 40 T. Mukherjee, 31 R. Naab, 65 R. Nagai, 16 M. Nakos, 40 U. Naumann, 64 J. Necker, 65 A. Negi, 4 L. Neste,⁵⁵ M. Neumann,⁴³ H. Niederhausen,²⁴ M. U. Nisa,²⁴ K. Noda,¹⁶ A. Noell,¹ A. Novikov,⁴⁴ A. Obertacke Pollmann,¹⁶ V. O'Dell,⁴⁰ B. Oeyen,²⁹ A. Olivas,¹⁹ R. Orsoe,²⁷ J. Osborn,⁴⁰ E. O'Sullivan,⁶³ H. Pandya,⁴⁴ N. Park, ³³ G. K. Parker, ⁴ E. N. Paudel, ⁴⁴ L. Paul, ⁵⁰ C. Pérez de los Heros, ⁶³ T. Pernice, ⁶⁵ J. Peterson, ⁴⁰ S. Philippen, ¹ A. Pizzuto, 40 M. Plum, 50 A. Pontén, 63 Y. Popovych, 41 M. Prado Rodriguez, 40 B. Pries, 24 R. Procter-Murphy, 19 G. T. Przybylski, 9 C. Raab, 37 J. Rack-Helleis, 41 M. Ravn, 63 K. Rawlins, 3 Z. Rechay, 40 A. Rehman, 44 P. Reichherzer, 11 E. Resconi, 27 S. Reusch, 65 W. Rhode, 23 B. Riedel, 40 A. Rifaie, 1 E. J. Roberts, 2 S. Robertson, 8,9 S. Rodan, 57,58 G. Roellinghoff,⁵⁷ M. Rongen,²⁶ A. Rosted,¹⁶ C. Rott,^{53,57} T. Ruhe,²³ L. Ruohan,²⁷ D. Ryckbosch,²⁹ I. Safa,⁴⁰ J. Saffer,³² D. Salazar-Gallegos,²⁴ P. Sampathkumar,³¹ A. Sandrock,⁶⁴ M. Santander,⁶⁰ S. Sarkar,²⁵ S. Sarkar,⁴⁷ J. Savelberg,¹ P. Savina, ⁴⁰ P. Schaile, ²⁷ M. Schaufel, ¹ H. Schieler, ³¹ S. Schindler, ²⁶ B. Schlüter, ⁴³ F. Schlüter, ¹² N. Schmeisser, ⁶⁴ T. Schmidt, ¹⁹ J. Schneider, ²⁶ F. G. Schröder, ^{31,44} L. Schumacher, ²⁶ S. Sclafani, ¹⁹ D. Seckel, ⁴⁴ M. Seikh, ³⁶ M. Seo, ⁵⁷ S. Seunarine, ⁵¹ P. Sevle Myhr, ³⁷ R. Shah, ⁴⁹ S. Shefali, ³² N. Shimizu, ¹⁶ M. Silva, ⁴⁰ B. Skrzypek, ⁸ B. Smithers, ⁴ R. Snihur, ⁴⁰ J. Soedingrekso, ²³ A. Søgaard, ²² D. Soldin, ⁵³ P. Soldin, ¹ G. Sommani, ¹¹ C. Spannfellner, ²⁷ G. M. Spiczak, ⁵¹ C. Spiering, ⁶⁵ D. Soldin, ⁵³ P. Soldin, ⁵⁴ P. Soldin, ⁵⁴ P. Soldin, ⁵⁵ P. Soldin, ⁵⁶ P. Sol M. Stamatikos, ²¹ T. Stanev, ⁴⁴ T. Stezelberger, ⁹ T. Stürwald, ⁶⁴ T. Stuttard, ²² G. W. Sullivan, ¹⁹ I. Taboada, ⁶ S. Ter-Antonyan, ⁷

A. Terliuk, ²⁷ M. Thiesmeyer, ¹ W. G. Thompson, ¹⁴ J. Thwaites, ⁴⁰ S. Tilav, ⁴⁴ K. Tollefson, ²⁴ C. Tönnis, ⁵⁷ S. Toscano, ¹² D. Tosi, ⁴⁰ A. Trettin, ⁶⁵ R. Turcotte, ³¹ J. P. Twagirayezu, ²⁴ M. A. Unland Elorrieta, ⁴³ A. K. Upadhyay, ^{40,*} K. Upshaw, ⁷ A. Vaidyanathan, ⁴² N. Valtonen-Mattila, ⁶³ J. Vandenbroucke, ⁴⁰ N. van Eijndhoven, ¹³ D. Vannerom, ¹⁵ J. van Santen, ⁶⁵ J. Vara, ⁴³ J. Veitch-Michaelis, ⁴⁰ M. Venugopal, ³¹ M. Vereecken, ³⁷ S. Verpoest, ⁴⁴ D. Veske, ⁴⁶ A. Vijai, ¹⁹ C. Walck, ⁵⁵ A. Wang, ⁶ C. Weaver, ²⁴ P. Weigel, ¹⁵ A. Weindl, ³¹ J. Weldert, ⁶² A. Y. Wen, ¹⁴ C. Wendt, ⁴⁰ J. Werthebach, ²³ M. Weyrauch, ³¹ N. Whitehorn, ²⁴ C. H. Wiebusch, ¹ D. R. Williams, ⁶⁰ J. Willison, ²⁴ L. Witthaus, ²³ A. Wolf, ¹ M. Wolf, ²⁷ G. Wrede, ²⁶ X. W. Xu, ⁷ J. P. Yanez, ²⁵ E. Yildizci, ⁴⁰ S. Yoshida, ¹⁶ R. Young, ³⁶ S. Yu, ^{24,53} T. Yuan, ⁴⁰ Z. Zhang, ⁵⁶ P. Zhelnin, ¹⁴ P. Zilberman, ⁴⁰ and M. Zimmerman ⁴⁰

(IceCube Collaboration)

```
<sup>1</sup>III. Physikalisches Institut, RWTH Aachen University, D-52056 Aachen, Germany
                          <sup>2</sup>Department of Physics, University of Adelaide, Adelaide, 5005, Australia
                          <sup>3</sup>Department of Physics and Astronomy, University of Alaska Anchorage,
                                  3211 Providence Drive, Anchorage, Alaska 99508, USA
                                  <sup>4</sup>Department of Physics, University of Texas at Arlington,
                    502 Yates Street, Science Hall Room 108, Box 19059, Arlington, Texas 76019, USA
                              <sup>5</sup>CTSPS, Clark-Atlanta University, Atlanta, Georgia 30314, USA
<sup>6</sup>School of Physics and Center for Relativistic Astrophysics, Georgia Institute of Technology, Atlanta, Georgia 30332, USA
                     Department of Physics, Southern University, Baton Rouge, Louisiana 70813, USA
                     <sup>8</sup>Department of Physics, University of California, Berkeley, California 94720, USA
                         Lawrence Berkeley National Laboratory, Berkeley, California 94720, USA
                      <sup>10</sup>Institut für Physik, Humboldt-Universität zu Berlin, D-12489 Berlin, Germany
                <sup>11</sup>Fakultät für Physik & Astronomie, Ruhr-Universität Bochum, D-44780 Bochum, Germany
                     <sup>12</sup>Université Libre de Bruxelles, Science Faculty CP230, B-1050 Brussels, Belgium
                         <sup>13</sup>Vrije Universiteit Brussel (VUB), Dienst ELEM, B-1050 Brussels, Belgium
            <sup>14</sup>Department of Physics and Laboratory for Particle Physics and Cosmology, Harvard University,
                                           Cambridge, Massachusetts 02138, USA
         <sup>15</sup>Department of Physics, Massachusetts Institute of Technology, Cambridge, Massachusetts 02139, USA
<sup>16</sup>Department of Physics and The International Center for Hadron Astrophysics, Chiba University, Chiba 263-8522, Japan
                     <sup>17</sup>Department of Physics, Loyola University Chicago, Chicago, Illinois 60660, USA
    <sup>18</sup>Department of Physics and Astronomy, University of Canterbury, Private Bag 4800, Christchurch, New Zealand
                    Department of Physics, University of Maryland, College Park, Maryland 20742, USA
                   <sup>20</sup>Department of Astronomy, The Ohio State University, Columbus, Ohio 43210, USA
        <sup>21</sup>Department of Physics and Center for Cosmology and Astro-Particle Physics, The Ohio State University,
                                                 Columbus, Ohio 43210, USA
                     <sup>22</sup>Niels Bohr Institute, University of Copenhagen, DK-2100 Copenhagen, Denmark
                     <sup>23</sup>Department of Physics, TU Dortmund University, D-44221 Dortmund, Germany
         <sup>24</sup>Department of Physics and Astronomy, Michigan State University, East Lansing, Michigan 48824, USA
                   <sup>25</sup>Department of Physics, University of Alberta, Edmonton, Alberta T6G 2E1, Canada
             <sup>26</sup>Erlangen Centre for Astroparticle Physics, Friedrich-Alexander-Universität Erlangen-Nürnberg,
                                                 D-91058 Erlangen, Germany
                    <sup>27</sup>Physik-department, Technische Universität München, D-85748 Garching, Germany
       <sup>28</sup>Département de physique nucléaire et corpusculaire, Université de Genève, CH-1211 Genève, Switzerland
                      Department of Physics and Astronomy, University of Gent, B-9000 Gent, Belgium
             <sup>30</sup>Department of Physics and Astronomy, University of California, Irvine, California 92697, USA
           <sup>31</sup>Karlsruhe Institute of Technology, Institute for Astroparticle Physics, D-76021 Karlsruhe, Germany
       <sup>32</sup>Karlsruhe Institute of Technology, Institute of Experimental Particle Physics, D-76021 Karlsruhe, Germany
 <sup>33</sup>Department of Physics, Engineering Physics, and Astronomy, Queen's University, Kingston, Ontario K7L 3N6, Canada
               <sup>34</sup>Department of Physics & Astronomy, University of Nevada, Las Vegas, Nevada 89154, USA
                 <sup>35</sup>Nevada Center for Astrophysics, University of Nevada, Las Vegas, Nevada 89154, USA
              <sup>36</sup>Department of Physics and Astronomy, University of Kansas, Lawrence, Kansas 66045, USA
         <sup>37</sup>Centre for Cosmology, Particle Physics and Phenomenology - CP3, Université catholique de Louvain,
                                                  Louvain-la-Neuve, Belgium
                      <sup>38</sup>Department of Physics, Mercer University, Macon, Georgia 31207-0001, USA
             <sup>39</sup>Department of Astronomy, University of Wisconsin—Madison, Madison, Wisconsin 53706, USA
    <sup>40</sup>Department of Physics and Wisconsin IceCube Particle Astrophysics Center, University of Wisconsin—Madison,
                                               Madison, Wisconsin 53706, USA
```

⁴¹Institute of Physics, University of Mainz, Staudinger Weg 7, D-55099 Mainz, Germany ⁴²Department of Physics, Marquette University, Milwaukee, Wisconsin 53201, USA ⁴³Institut für Kernphysik, Westfälische Wilhelms-Universität Münster, D-48149 Münster, Germany ⁴⁴Bartol Research Institute and Department of Physics and Astronomy, University of Delaware, Newark, Delaware 19716, USA ⁴⁵Department of Physics, Yale University, New Haven, Connecticut 06520, USA ⁴⁶Columbia Astrophysics and Nevis Laboratories, Columbia University, New York, New York 10027, USA ⁴⁷Department of Physics, University of Oxford, Parks Road, Oxford OX1 3PU, United Kingdom ⁴⁸Dipartimento di Fisica e Astronomia Galileo Galilei, Università Degli Studi di Padova, I-35122 Padova PD, Italy Department of Physics, Drexel University, 3141 Chestnut Street, Philadelphia, Pennsylvania 19104, USA ⁵⁰Physics Department, South Dakota School of Mines and Technology, Rapid City, South Dakota 57701, USA Department of Physics, University of Wisconsin, River Falls, Wisconsin 54022, USA ⁵²Department of Physics and Astronomy, University of Rochester, Rochester, New York 14627, USA ³Department of Physics and Astronomy, University of Utah, Salt Lake City, Utah 84112, USA ⁵⁴Department of Physics, Chung-Ang University, Seoul 06974, Republic of Korea ⁵⁵Oskar Klein Centre and Department of Physics, Stockholm University, SE-10691 Stockholm, Sweden ⁵⁶Department of Physics and Astronomy, Stony Brook University, Stony Brook, New York 11794-3800, USA ⁵⁷Department of Physics, Sungkyunkwan University, Suwon 16419, Republic of Korea ⁵⁸Institute of Basic Science, Sungkyunkwan University, Suwon 16419, Republic of Korea ⁵⁹Institute of Physics, Academia Sinica, Taipei, 11529, Taiwan ⁶⁰Department of Physics and Astronomy, University of Alabama, Tuscaloosa, Alabama 35487, USA ⁶¹Department of Astronomy and Astrophysics, Pennsylvania State University, University Park, Pennsylvania 16802, USA ⁵²Department of Physics, Pennsylvania State University, University Park, Pennsylvania 16802, USA ⁶³Department of Physics and Astronomy, Uppsala University, Box 516, SE-75120 Uppsala, Sweden ⁶⁴Department of Physics, University of Wuppertal, D-42119 Wuppertal, Germany ⁶⁵Deutsches Elektronen-Synchrotron DESY, Platanenallee 6, D-15738 Zeuthen, Germany

(Received 3 May 2024; revised 11 October 2024; accepted 2 January 2025; published 7 March 2025)

The DeepCore subdetector of the IceCube Neutrino Observatory provides access to neutrinos with energies above approximately 5 GeV. Data taken between 2012 and 2021 (3387 days) are utilized for an atmospheric ν_{μ} disappearance analysis that studied 150 257 neutrino-candidate events with reconstructed energies between 5 and 100 GeV. An advanced reconstruction based on a convolutional neural network is applied, providing increased signal efficiency and background suppression, resulting in a measurement with both significantly increased statistics compared to previous DeepCore oscillation results and high neutrino purity. For the normal neutrino mass ordering, the atmospheric neutrino oscillation parameters and their 1σ errors are measured to be $\Delta m_{32}^2 = 2.40^{+0.05}_{-0.04} \times 10^{-3} \text{ eV}^2$ and $\sin^2\theta_{23} = 0.54^{+0.04}_{-0.03}$. The results are the most precise to date using atmospheric neutrinos, and are compatible with measurements from other neutrino detectors including long-baseline accelerator experiments.

DOI: 10.1103/PhysRevLett.134.091801

Published by the American Physical Society under the terms of the Creative Commons Attribution 4.0 International license. Further distribution of this work must maintain attribution to the author(s) and the published article's title, journal citation, and DOI. Funded by SCOAP³.

Introduction—The discovery of neutrino oscillations [1,2] triggered significant experimental effort over the course of the past quarter century to confirm and subsequently measure with increasing precision the properties that describe neutrino flavor oscillations [3]. These oscillations result from the mixing between neutrino mass and flavor states described by the Pontecorvo-Maki-Nakagawa-Sakata (PMNS) mixing matrix [4,5] (often parametrized as three mixing angles and a *CP*-violation phase), and differences between the masses of the states. For GeV-scale atmospheric neutrinos, flavor oscillations occur primarily between the muon and tau flavors, driven by the mixing angle θ_{23} and the mass splitting of the neutrino states Δm_{atm}^2 (where $\Delta m_{\rm atm}^2 \equiv \Delta m_{32}^2$ for the normal neutrino mass ordering). The probability for these neutrino oscillations may be

^{*}Also at Institute of Physics, Sachivalaya Marg, Sainik School Post, Bhubaneswar 751005, India.

[†]Also at Department of Space, Earth and Environment, Chalmers University of Technology, 412 96 Gothenburg, Sweden.

[‡]Also at Earthquake Research Institute, University of Tokyo, Bunkyo, Tokyo 113-0032, Japan.

^{*}Present address: Institute for Artificial Intelligence and Fundamental Interactions, Massachusetts Institute of Technology, 77 Massachusetts Avenue, 26-555, Cambridge, Massachusetts, USA.

Contact author: analysis@icecube.wisc.edu

Present address: Department of Physics, Simon Fraser University, Burnaby, BC V5A 1S6, Canada.

approximated by a vacuum transition of muon to tau flavor of the form

$$P(\nu_{\mu} \to \nu_{\tau}) \approx \sin^2(2\theta_{23})\sin^2\left(\frac{\Delta m_{\text{atm}}^2 L}{4E}\right),$$
 (1)

where L is the distance the neutrino traveled, and E is the energy of the neutrino. Increasingly precise experimental constraints on the mass splittings and PMNS elements allow stringent tests of the current 3ν paradigm with any deviation potentially revealing the influence of new physics in neutrino oscillations [6].

Atmospheric neutrinos produced by cosmic-ray interactions in Earth's atmosphere create a natural source of neutrinos arriving from all directions [7–9] with baselines (L) varying from $\mathcal{O}(10\text{--}10\,000)$ km. Events arriving from below the local horizon, as in the case of the neutrino data sample considered here, travel sufficient distance for neutrino oscillations to be observed, providing the strongest signal, while mitigating dominant downward-going atmospheric muon backgrounds. Vertically up-going Earth-crossing neutrinos traversing approximately 1.3×10^4 km result in nearly complete ν_{μ} disappearance for energies of $\mathcal{O}(10~\text{GeV})$.

In this Letter, we present a measurement of Δm_{32}^2 and $\sin^2(\theta_{23})$ leveraging the statistical power available with 9.3 years of IceCube DeepCore data. The oscillation signal extraction follows that applied in [10] where a histogram of reconstructed detector data is compared to a simulationbased template histogram that is reweighted based on free parameters in the fit. Calibration and event selection improvements reported in [10], applied here, are further improved by convolutional-neural-network- (CNN) based reconstruction methods. The previous reconstruction methods could only be applied to a relatively small subsample of signal-like events to ensure high-quality reconstruction performance. In contrast, the CNN-based reconstruction methods described here provide an approximate 5000× decrease in the event processing time and robust interpretations of all event types in the evaluated dataset. A significant increase in neutrino candidates compared to previous DeepCore oscillation results is realized. Combined with nearly two additional years of detector data, this measurement benefits from a nearly sevenfold increase in statistics compared to the previous most sensitive oscillation measurement from DeepCore [10]. The increased statistics of the study also allow more precise constraints to be placed on systematic uncertainties, resulting in the most precise measurement of oscillations with atmospheric neutrinos to date.

The IceCube DeepCore detector—The IceCube Neutrino Observatory [11] instruments more than a cubic km of the glacial ice sheet at the geographic South Pole. A total of 5160 digital optical modules (DOMs) [12], each containing a single 10-in. photomultipier tube [13], are deployed on

86 vertical "strings" within the instrumented volume. These DOMs detect Cherenkov light resulting from the charged particles produced by neutrino interactions in the ice. A primary high-energy array of 78 strings optimized for detection of events above $\mathcal{O}(100 \text{ GeV})$ is deployed on an approximately triangular grid with a string-to-string spacing of 125 m and a vertical DOM spacing of 17 m. The central region of the detector is more densely instrumented with eight additional strings creating the DeepCore subarray [14]. The DeepCore subarray has an average stringto-string spacing of $\mathcal{O}(50 \text{ m})$ and vertical DOM spacing of 7 m, with the DOMs concentrated below 2100 m where the ice is the clearest and has the best optical properties. The 10-Mton DeepCore volume has detection sensitivity to neutrinos in the (5–100)-GeV energy range where neutrino oscillations are observable.

Detected Cherenkov photons are converted into digitized electronic pulses from which charge and timing information are extracted. These "hits" are the input data used to reconstruct the properties of the interacting neutrino, and discriminate neutrinos from random detector noise and atmospheric muon backgrounds.

Reconstruction and event selection—A key element in this measurement is the CNN-based reconstruction [15] modeled on previously successful image classification and reconstruction for TeV-scale IceCube events [16]. The new CNN reconstruction consists of five independent neural networks optimized for each reconstruction task using $\mathcal{O}(10-100 \text{ GeV})$ -scale IceCube DeepCore neutrino events [17,18]. All networks use the same architecture, with two parallel branches of eight convolutional layers each, which combine into a single dense layer that outputs the desired feature(s). Each of the input branches takes in five summary variables from all 60 DOMs on either the eight DeepCore strings or the 19 centermost IceCube strings. While DOMs with multiple hits per event are rarer at the GeV scale, this can still occur, particularly in the important region near the neutrino interaction vertex. Thus, the five summary variables are the sum of the charge, time of the first hit, time of the last hit, charge-weighted mean of the times of hits, and charge-weighted standard deviation of the times of hits, where a minimum charge of 0.25 photoelectrons is requested to be considered as a hit. These summary variables allow the network to account for multiple hits per DOM per event, with emphasis on the first and last hits, but also include additional information in the last two variables to account for the fact that those hits could be influenced by noise. The variables only use hits within [-500, 4000] ns of the DeepCore trigger [14] to avoid noise contamination in the event.

The CNNs are trained separately for neutrino energy, incoming neutrino angle with respect to the zenith (θ_{zenith}), interaction vertex position (x, y, z), particle identification (PID) based on event shape, and classifying atmospheric muons. Each network is trained on a specifically designed

sample that is independent of the analysis sample. Each sample is optimized to have a flat distribution across the target regression variables or equal sample sizes between the binary classification labels. In addition, no physical weights were used, such that the training is not biased by the expected distribution or physics models. Monte Carlo (MC) datasets for training are simulated using the same MC models applied in the analysis. The energy, zenith, and vertex CNNs are trained on simulated ν_{μ} charged-current (CC) tracklike events since these are the most important for the oscillation measurement. The network for reconstructing the zenith angle is trained on a sample of approximately $5 \times 10^6 \nu_u$ CC MC events with a flat true zenith angle distribution, true neutrino energies between 5 and 300 GeV, and with starting and ending points within the near-DeepCore region (a depth of -495 to -225 m in detector coordinates and radius within 200 m relative to the centermost IceCube string). The networks for reconstructing neutrino energy and interaction vertex are trained on a larger ν_{μ} CC dataset of 9×10^6 events with a flat simulated energy distribution below 200 GeV, and moderately extended to higher energies with a falling shoulder. Events that have hits on fewer than seven DOMs are excluded from the training samples. After training on the specifically designed training samples, the performance was evaluated on other event types (such as ν_e CC events) with realistic, physical spectrum to demonstrate acceptable performance. Figure 1 provides the resultant zenith and

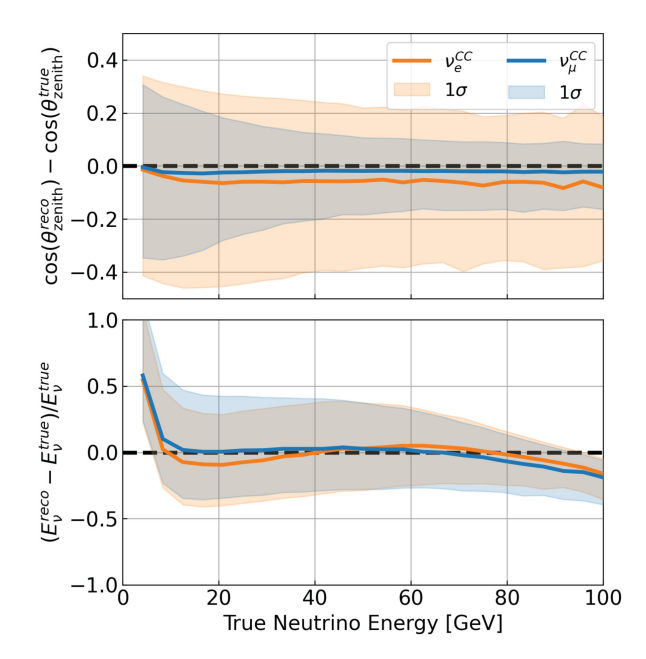


FIG. 1. Reconstruction resolution of $\cos(\theta_{\text{zenith}})$ (top) and neutrino energy (bottom) compared to the true neutrino energy. For ν_{μ} CC events (blue) and ν_{e} CC events (orange), the median is indicated by the solid curve, and the 1σ region is shown as a shaded band. The observed resolutions are similar to those realized in traditional log-likelihood methods [19].

energy resolutions of the trained CNN reconstructions for ν_{μ} CC and ν_{e} CC analysis-level events.

The PID and atmospheric muon classifiers are trained using MC neutrino events with true neutrino energy between 5 and 200 GeV for the best performance in the low-energy region. The PID discriminator is trained on a sample of balanced tracklike (ν_{μ} CC) and cascadelike [ν_e CC, ν_e neutral current (NC), and ν_μ NC] events using a total of 5×10^6 events for training. The atmospheric muon classifier, for which all events are required to have hits on at least four DOMs, is trained on a subsample of the neutrino MC used for the PID network and an additional 2.8×10^6 muon events. The ratio of atmospheric ν_e : ν_μ : μ of this training sample is 1:2:2. To optimize the rejection of misreconstructed muon events (see Ref. [20]), a boosted decision tree (BDT) is trained on the events after a cut on reconstructed zenith angle that requires $\cos(\theta_{\text{zenith}}) \le 0.3$ using the CNN atmospheric muon classifier along with other reconstructed variables describing positional information of neutrino candidates as input. These variables include the depth (z) and radius (relative to the central IceCube string) of the CNNreconstructed event interaction vertex, a low-level muon BDT classifier (see Fig. 7 of [10]), and the z coordinate of the deepest corridor hit (see Fig. 2 of [10]).

The applied data and MC sample of this analysis begins with the DeepCore Common Data Sample described in Sec. III of [10], which reduces the atmospheric muon background and detector noise to achieve a neutrinodominated sample. The CNN reconstructions are then applied to the DeepCore Common Data Sample, along with a few additional final level cuts. Events are only selected if the following containment cuts are satisfied: the reconstructed neutrino interaction vertex is contained in DeepCore, the reconstructed energy is between 5 and 100 GeV, and the reconstructed $\cos(\theta_{\text{zenith}})$ is below 0.04, indicating that the incoming neutrino arrived from near or below the horizon. To remove independent muon events that occur coincidentally in the same time window, we require no recorded hit in the top 15 layers of IceCube DOMs and no more than seven detected hits in the outermost IceCube strings. Maintaining that at least three DOMs observe direct hits from unscattered photons [21] effectively filters random coincidences of radioactive decay noise and events with poor reconstruction performance. To achieve the best performance of the CNNs, we keep only the events with at least seven hits on DOMs in and near DeepCore. Finally, applying the BDT classifier described above for a score ≥ 0.8 provides a final rate for the atmospheric muon background that is well below 1% of the entire sample (see Table I). We achieve a neutrino-rich sample with good reconstruction resolution in the region sensitive to oscillation parameter measurements.

A kernel density estimator [10] is ultimately employed to smooth the expected atmospheric muon background

TABLE I. The expected MC events (integer values) compared to the data sample, for the best fit to the data considering neutrino interaction type and atmospheric muons.

	$N_{\text{events}}(9.3 \text{ yr})$	% of MC sample	
$\overline{\nu_{\mu} \text{ CC}}$	88 306	58.8	
ν_e CC	35 296	23.5	
ν_{τ} CC	8772	5.8	
ν NC	16 981	11.3	
Atmospheric μ	917	0.6	
Total MC	150 272		
Data	150 257		

distribution in the final MC sample due to the low statistics in most analysis bins.

The selected sample is binned (see Fig. 2) by reconstructed energy in ten logarithmically spaced bins from 5 to 100 GeV, eight linear-spaced bins of $\cos(\theta_{zenith})$ between [-,0.04], and three PID bins with bin edges of [0,0.25,0.55,1]. As indicated in Eq. (1), the probability of oscillation is dependent on the neutrino's distance traveled (calculated from zenith angle) and energy. Thus, deficits from muon neutrino oscillation should be visible when the counts are plotted as a function of the energy and baseline. Here, ν_{μ} CC events largely occupy the tracklike bin, and other types of neutrino interactions, mostly classified as cascadelike, have quite different detector response, and cross sections [22]. Applying the PID binning, where the highest score indicates the most tracklike or ν_{μ} CC events, divides the sample by flavor (see Ref. [20]). The ν_{μ} CC

disappearance signature due to oscillations is strongest in the last PID bin, which has the highest ν_{μ} CC purity (see Figs. 2 and 3).

Analysis—Models of the systematic uncertainties largely follow those presented in [10]. A summary of the systematic uncertainties is provided in the End Matter section, with further details in [20]. The sample used in [10] includes only the most tracklike events divided into two PID bins, and it did not include the cascadelike events. This analysis retains all neutrino flavor and interaction types and therefore contains more cascadelike events than [10]. This additional off-signal region is useful for constraining systematic uncertainties, along with including energies above where oscillations are expected (see Ref. [20]).

Identified nuisance parameters of the analysis are fit together with the oscillation parameters to the data using a log-likelihood (LLH) as the test statistic of the form:

LLH =
$$\sum_{i \in \text{bins}} \log \left(\frac{n_i^{n_o} e^{-n_i}}{n_o!} \right) - \frac{1}{2} \sum_{j \in \text{syst}} \frac{(\hat{s}_j - s_j)^2}{\sigma_j^2}.$$
 (2)

Here the first term is a Poisson likelihood where n_i (n_o) is the number of expected (observed) events in bin i, and the second term serves as a penalty term for the systematic parameters j which have Gaussian priors σ_j . The results of the fitted nuisance parameters to their priors are shown in End Matter Appendix A (and [20]) and discussed next.

Results and conclusion—An atmospheric neutrino dataset obtained over 3,387 days between 2012 and 2021, with a total of 150 257 neutrino candidates, has been used in this

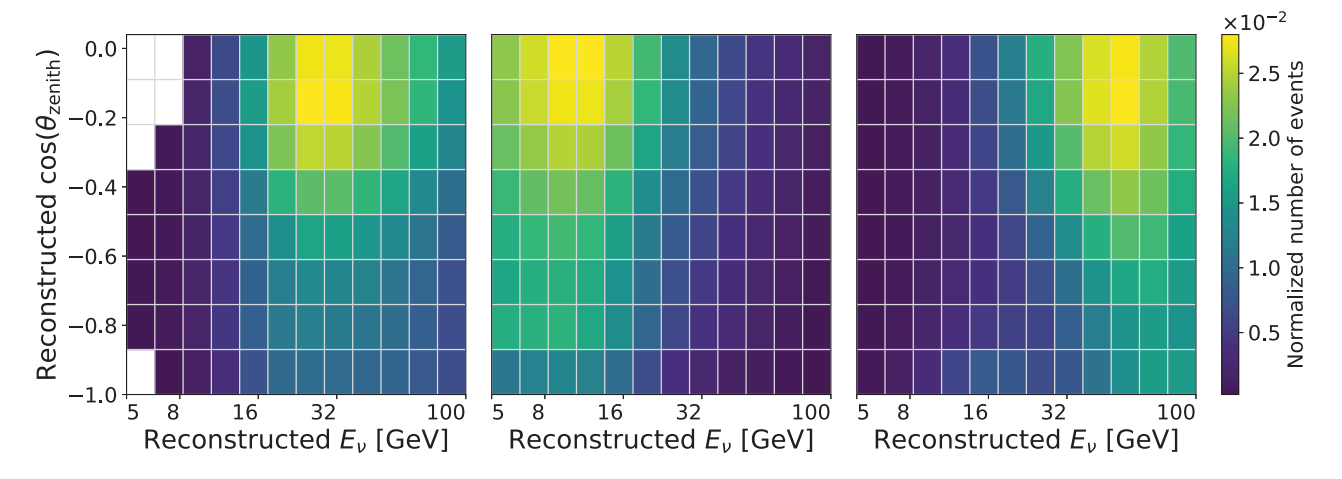


FIG. 2. The nominal MC distributions for the analysis sample binned logarithmically in reconstructed energy and linearly in cosine of the reconstructed zenith angle. Each histogram represents one PID bin selected by the range of the event PID score (from left to right): 0–0.25 (cascadelike), 0.25–0.55 (cascadelike and tracklike), and 0.55–1.0 (track-like). At lower energies, ν_{μ} CC events produce shorter tracks that are more challenging to identify, resulting in these events populating the center panel and a peak of those events at lower energies. Similarly at higher energies, these events produce longer muon tracks that are more readily identified, placing these events in the right panel and peaking at higher energies. The oscillation signature region is observable in this distribution via the dark diagonal band. The left panel contains both event types, causing the distribution to peak at intermediate energies. The total number of events are taken from Table 1 with a ratio of 22 991:99 931:27 350. Bins containing very low statistics in data or MC are not used in the analysis.

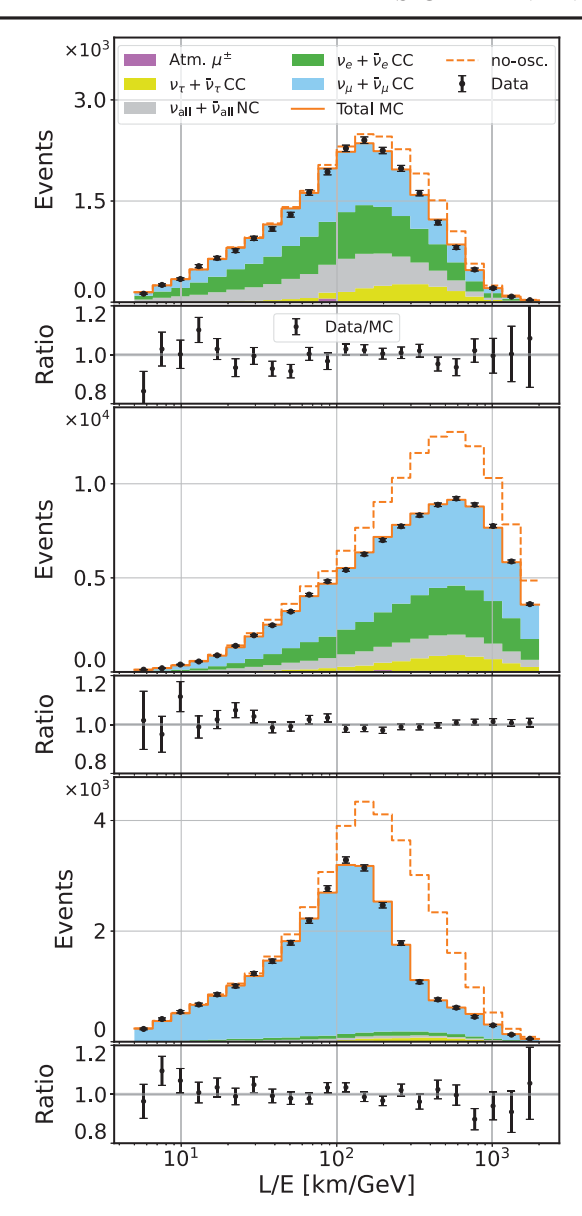


FIG. 3. Comparative distributions of observed event data to the MC as a function of the ratio of reconstructed neutrino baseline (L) to energy (E) with error bars showing the Poisson statistical error of data. Shown in the panels top to bottom are each of the PID score bins: 0–0.25 (cascadelike), 0.25–0.55 (track- and cascadelike), and 0.55–1.0 (tracklike). The dashed histograms show the MC distributions with best-fit parameters, with the absence of ν_{μ} disappearance ($\theta_{23} = 0$).

analysis. The most tracklike bin has highest purity of ν_{μ} CC events and shows the most distinctive disappearance signature. We obtain a goodness-of-fit p value of 19.2%. All nuisance parameters fitted to values well within their expected ranges (see Ref. [20]).

To determine the confidence intervals for the oscillation parameters, the Feldman-Cousins's unified approach [23,24] is used for all errors and plots by sampling pseudo-data trials from the best-fit values with Poisson fluctuation applied to each analysis bin. We report the

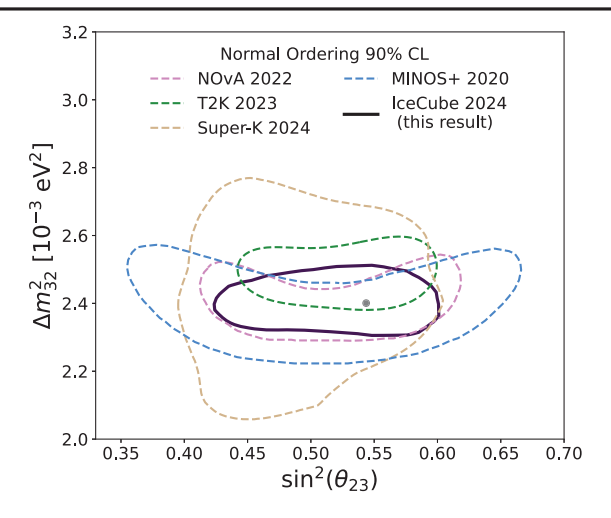


FIG. 4. Contours showing Feldman-Cousins 90% CL assuming neutrino normal mass ordering of this analysis (black, "IceCube 2024") compared to those from NOvA [26], T2K [27], Super-Kamiokande [28], and MINOS+ [29]. The best-fit physics parameters are indicated with a black circle. It is noted the Wilks's theorem [30] likelihood maps associated with this result are provided in [25].

parameters and 1σ errors of $\Delta m_{32}^2 = 2.40^{+0.05}_{-0.04} \times 10^{-3} \text{ eV}^2$ and $\sin^2(\theta_{23}) = 0.54^{+0.04}_{-0.03}$ in the normal neutrino mass ordering. The 90% confidence level (CL) contour of $\sin^2(\theta_{23})$ and Δm_{32}^2 for the normal neutrino mass ordering $(m_3 > m_2 > m_1)$ of this result, compared with the results from the other experiments, is shown in Fig. 4. It is noted that results for the inverted mass ordering case are provided in [25].

This result presents an important transition for IceCube DeepCore atmospheric neutrino oscillation measurements to a systematics-uncertainty-dominated regime [20]. The reported precision is similar to and consistent with measurements from accelerator and reactor [31] neutrino experiments while uniquely using neutrinos of much higher energy over longer baselines, supporting the standard 3ν paradigm of neutrino mixing. The upcoming IceCube Upgrade [32] next-generation detector implementing a denser configuration of next-generation detector modules and advanced calibration instrumentation will enable significant improvements to this measurement in the coming decade.

Acknowledgments—The authors gratefully acknowledge the support from the following agencies and institutions: (USA) U.S. National Science Foundation-Office of Polar Programs, U.S. National Science Foundation-Physics Division, U.S. National Science Foundation-EPSCoR, U.S. National Science Foundation-Office of Advanced Cyberinfrastructure, U.S. National Science Foundation AI Institute for Artificial Intelligence and Fundamental Interactions, Wisconsin Alumni Research Foundation, Center for High Throughput Computing at

the University of Wisconsin-Madison, Open Science Grid, Partnership to Advance Throughput Computing, Advanced Cyberinfrastructure Coordination Ecosystem: Services & Support, Frontera computing project at the Texas Advanced Computing Center, U.S. Department of Energy National Energy Research Scientific Computing Center, Particle astrophysics research computing center at the University of Maryland, Institute for Cyber-Enabled Research at Michigan State University, Astroparticle physics computational facility at Marquette University, NVIDIA Corporation, and Google Cloud Platform; (Belgium) Funds for Scientific Research (FRS-FNRS and FWO), FWO Odysseus and Big Science programs, and Belgian Federal Science Policy Office; (Germany) Bundesministerium für Bildung und Forschung, Deutsche Forschungsgemeinschaft, Helmholtz Alliance Astroparticle Physics, Initiative and Networking Fund of the Helmholtz Association, Deutsches Elektronen Synchrotron, and High Performance Computing cluster of the RWTH Aachen; (Sweden) Swedish Research Council, Swedish Polar Research Secretariat, Swedish National Infrastructure for Computing, and Knut and Alice Wallenberg Foundation; (European Union) EGI Advanced Computing for research; (Australia) Australian Research Council; (Canada) Natural Sciences and Engineering Research Council of Canada, Calcul Québec, Compute Ontario, Canada Foundation for Innovation, WestGrid, and Digital Research Alliance of Canada; (Denmark) Villum Fonden, Carlsberg Foundation, and European Commission; (New Zealand) Marsden Fund; (Japan) Japan Society for Promotion of Science and Institute for Global Prominent Research of Chiba University; (Korea) National Research Foundation of Korea; (Switzerland) Swiss National Science Foundation.

Data availability—The numerical data associated with the presented results are available in [25].

- [1] Y. Fukuda *et al.* (Super-Kamiokande Collaboration), Evidence for oscillation of atmospheric neutrinos, Phys. Rev. Lett. **81**, 1562 (1998).
- [2] Q. R. Ahmad *et al.* (SNO Collaboration), Measurement of the rate of $\nu_e + d \rightarrow p + p + e^-$ interactions produced by 8B solar neutrinos at the Sudbury Neutrino Observatory, Phys. Rev. Lett. **87**, 071301 (2001).
- [3] R. L. Workman and Others (Particle Data Group), Review of particle physics, Prog. Theor. Exp. Phys. 2022, 083C01 (2022).
- [4] B. Pontecorvo, Mesonium and anti-mesonium, Sov. Phys. J. Exp. Theor. Phys. **6**, 429 (1957).
- [5] Z. Maki, M. Nakagawa, and S. Sakata, Remarks on the unified model of elementary particles, Prog. Theor. Phys. 28, 870 (1962).
- [6] P. B. Denton, M. Friend, M. D. Messier, H. A. Tanaka, S. Böser, J. A. B. Coelho, M. Perrin-Terrin, and T. Stuttard,

- Snowmass neutrino frontier: NF01 topical group report on three-flavor neutrino oscillations, arXiv:2212.00809.
- [7] L. V. Volkova, Energy spectra and angular distributions of atmospheric neutrinos, Sov. J. Nucl. Phys. **31**, 784 (1980).
- [8] G. D. Barr, T. K. Gaisser, P. Lipari, S. Robbins, and T. Stanev, Three-dimensional calculation of atmospheric neutrinos, Phys. Rev. D 70, 023006 (2004).
- [9] M. Honda, M. S. Athar, T. Kajita, K. Kasahara, and S. Midorikawa, Atmospheric neutrino flux calculation using the NRLMSISE-00 atmospheric model, Phys. Rev. D 92, 023004 (2015).
- [10] R. Abbasi *et al.* (IceCube Collaboration), Measurement of atmospheric neutrino mixing with improved IceCube DeepCore calibration and data processing, Phys. Rev. D **108**, 012014 (2023).
- [11] M. G. Aartsen *et al.* (IceCube Collaboration), The IceCube Neutrino Observatory: Instrumentation and online systems, J. Instrum. **12**, P03012 (2017).
- [12] R. Abbasi et al. (IceCube Collaboration), The IceCube data acquisition system: Signal capture, digitization, and timestamping, Nucl. Instrum. Methods Phys. Res., Sect. A 601, 294 (2009).
- [13] R. Abbasi *et al.*, Calibration and characterization of the IceCube photomultiplier tube, Nucl. Instrum. Methods Phys. Res., Sect. A **618**, 139 (2010).
- [14] R. Abbasi *et al.* (IceCube Collaboration), The design and performance of IceCube DeepCore, Astropart. Phys. **35**, 615 (2012).
- [15] A. Krizhevsky, I. Sutskever, and G. Hinton, ImageNet classification with deep convolutional neural networks, Commun. ACM **60**, 84 (2017).
- [16] R. Abbasi *et al.*, A convolutional neural network based cascade reconstruction for the IceCube Neutrino Observatory, J. Instrum. **16**, P07041 (2021).
- [17] J. Micallef, Measurement of atmospheric muon neutrino disappearance with IceCube using convolutional neural network reconstructions, Ph.D. thesis, ProQuest, 2022.
- [18] S. Yu *et al.*, Measurement of atmospheric muon neutrino disappearance using CNN reconstructions with IceCube, Phys. Sci. Forum **8**, 62 (2023).
- [19] M. G. Aartsen *et al.* (IceCube Collaboration), Measurement of atmospheric tau neutrino appearance with IceCube DeepCore, Phys. Rev. D **99**, 032007 (2019).
- [20] See Supplemental Material at http://link.aps.org/supplemental/10.1103/PhysRevLett.134.091801 for the data of the experiments.
- [21] R. Abbasi *et al.* (IceCube Collaboration), Low energy event reconstruction in IceCube DeepCore, Eur. Phys. J. C 82, 807 (2022).
- [22] J. Tena-Vidal, C. Andreopoulos, A. Ashkenazi, C. Barry, S. Dennis, S. Dytman *et al.* (GENIE Collaboration), Neutrinonucleon cross-section model tuning in GENIE v3, Phys. Rev. D 104, 072009 (2021).
- [23] G. J. Feldman and R. D. Cousins, Unified approach to the classical statistical analysis of small signals, Phys. Rev. D 57, 3873 (1998).
- [24] A. Sousa, N. Buchanan, S. Calvez, P. Ding, D. Doyle, A. Himmel, B. Holzman, J. Kowalkowski, A. Norman, and T. Peterka, Implementation of Feldman-Cousins corrections and oscillation calculations in the HPC environment for

- the NOvA Experiment, EPJ Web Conf. **214**, 05012 (2019).
- [25] Icecube Collaboration data archive, https://icecube.wisc.edu/data-releases/2024/09/neutrino-oscillation-parameters-using-convolutional-neural-networks-with-9-3-years-of-data-in-icecube-deepcore/.
- [26] M. A. Acero *et al.* (NOvA Collaboration), Improved measurement of neutrino oscillation parameters by the NOvA experiment, Phys. Rev. D 106, 032004 (2022).
- [27] K. Abe *et al.* (T2K Collaboration), Measurements of neutrino oscillation parameters from the T2K experiment using 3.6×10^{21} protons on target, Eur. Phys. J. C **83**, 782 (2023).
- [28] T. Wester *et al.* (The Super-Kamiokande Collaboration), Atmospheric neutrino oscillation analysis with neutron tagging and an expanded fiducial volume in Super-Kamiokande I–V, Phys. Rev. D **109**, 072014 (2024).
- [29] P. Adamson *et al.* (MINOS+ Collaboration), Precision constraints for three-flavor neutrino oscillations from the full MINOS+ and MINOS dataset, Phys. Rev. Lett. 125, 131802 (2020).
- [30] S. S. Wilks, The large-sample distribution of the likelihood ratio for testing composite hypotheses, Ann. Math. Stat. 9, 60 (1938).
- [31] F. P. An *et al.* (Daya Bay Collaboration), Precision measurement of reactor antineutrino oscillation at kilometer-scale

- baselines by Daya Bay, Phys. Rev. Lett. **130**, 161802 (2023).
- [32] P. Eller *et al.* (IceCube Collaboration), Sensitivity of the IceCube Upgrade to atmospheric neutrino oscillations, Proc. Sci., ICRC2023 (**2023**) 1036.
- [33] P. Eller et al. (IceCube Collaboration), A model independent parametrization of the optical properties of the refrozen IceCube drill holes, Proc. Sci., ICRC2023 (2023) 1034.
- [34] R. Abbasi *et al.*, In situ estimation of ice crystal properties at the South Pole using LED calibration data from the IceCube Neutrino Observatory, Cryosphere **18**, 75 (2024).
- [35] D. Chirkin (IceCube Collaboration), Evidence of optical anisotropy of the South Pole ice, in *Proceedings of the 33rd ICRC* (2013), p. 0580, arXiv:1309.7010.
- [36] G. D. Barr, S. Robbins, T. K. Gaisser, and T. Stanev, Uncertainties in atmospheric neutrino fluxes, Phys. Rev. D 74, 094009 (2006).
- [37] A. Fedynitch, F. Riehn, R. Engel, T. K. Gaisser, and T. Stanev, Hadronic interaction model SIBYLL 2.3c and inclusive lepton fluxes, Phys. Rev. D **100**, 103018 (2019).
- [38] A. Cooper-Sarkar, P. Mertsch, and S. Sarkar, The high energy neutrino cross-section in the Standard Model and its uncertainty, J. High Energy Phys. 08 (2011) 042.

End Matter

Appendix A: Systematic uncertainties—The models to describe the sources of systematic uncertainty draw from [10], with some modifications. Uncertainty in the photon detection efficiency is characterized by an absolute DOM efficiency scale and two relative efficiencies based on the photon incidence angle with respect to the DOMs ("Relative efficiency p_0 ," "Relative efficiency p_1 ") that account for the local properties of the refrozen ice near the sensors following installation [33]. Uncertainty in the "scattering" and "absorption" properties of the

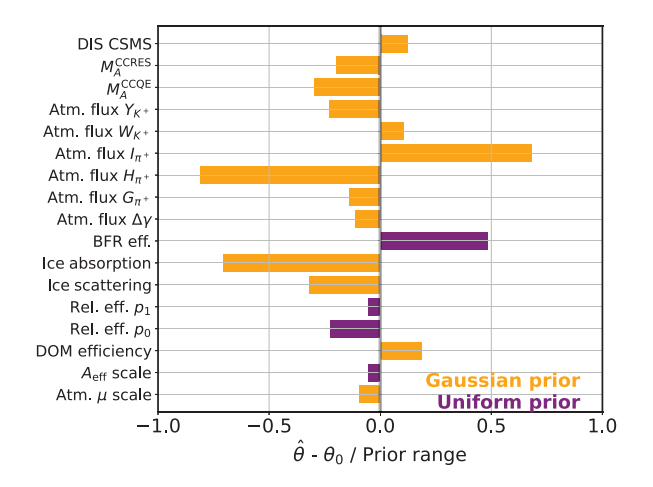


FIG. 5. Showing the pulls for the systematic uncertainty parameters compared with the ranges of their priors of the data analysis.

undisturbed bulk glacial ice are also included. Furthermore, a new calibration model accounting for the birefringent polycrystalline microstructure of the ice [34] has been introduced to describe the azimuthal anisotropy observed in the ice. We employed a new systematic parameter ("BFR eff.") in this analysis that interpolates between this new model and the previous baseline model where the anisotropy was accounted for by an empirical model (SPICE-3.2.1 [35]).

Conservative uncertainties in the atmospheric neutrino flux as defined in [36] were adopted with their impact evaluated using the MCEq software package [37]. Two (three) effective parameters describing kaon (pion) production during cosmic-ray interactions with nuclei in the atmosphere are varied in the analysis, in addition to an overall uncertainty in the power law spectral index $(\Delta \gamma_{\nu})$. The overall normalization of both the neutrino ("A_{eff} scale") and muon ("atmospheric μ scale") rates are also fit parameters, meaning the oscillation parameter measurement is independent of the absolute atmospheric flux. Uncertainties in the neutrino-ice cross section due to axial currents in the quasielastic and resonance channels (" $M_A^{CCQE/RES}$ ") are included, and interpolation is done between the GENIE [22] (low-energy) and CSMS [38] (high-energy) deep inelastic scattering (DIS) cross-section models in the analysis energy range ("DIS CSMS").

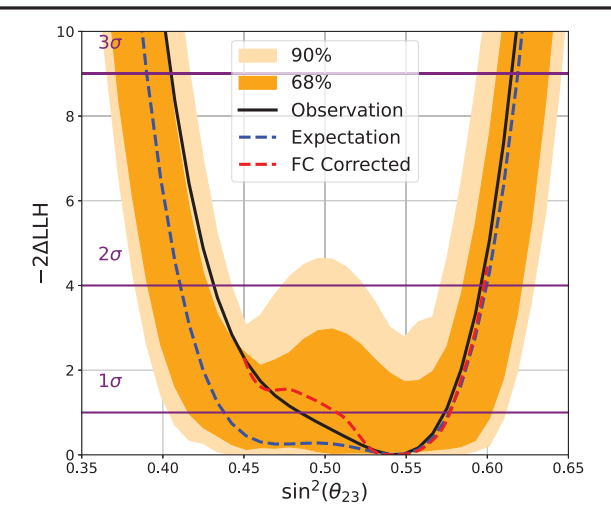
Additional information about the 17 systematic parameters that are included as nuisance parameters in the fit is provided in Fig. 5 and in Table II. Each parameter has a

TABLE II. The systematic uncertainty parameters included as nuisance parameters in the data analysis, along with their associated priors. The priors on parameters can either be Gaussian (in which case, the value corresponding to $\pm 1\sigma$ is listed) or uniform (in which case, the allowed range is listed).

Parameter	Nominal	Prior width	Fit valuePull (σ)		
Detector:					
DOM efficiency	+0%	$\pm 10\%$	+1.8%	0.18	
Ice absorption	+0%	$\pm 5\%$	-3.5%	-0.71	
Ice scattering	+5%	$\pm 10\%$	+1.8%	-0.32	
Relative efficiency p	0.10	[-0.6, 0.5]	-0.14		
Relative efficiency p	-0.05	[-0.2, 0.2]	-0.07		
BFR efficiency	0.0	[0, 1]	0.48		
Atmospheric flux:					
$\Delta\gamma_ u$	0.0	± 0.1	-0.011	-0.11	
$\Delta\pi^{\pm}$ yields I	0.0	$\pm 61\%$	+42%	0.68	
$\Delta\pi^{\pm}$ yields G	0.0	$\pm 30\%$	-4.2%	-0.14	
$\Delta\pi^{\pm}$ yields H	0.0	$\pm 15\%$	-12%	-0.81	
ΔK^+ yields W	0.0	$\pm 40\%$	+4.2%	0.11	
ΔK^+ yields Y	0.0	$\pm 30\%$	-6.9%	-0.23	
Cross section:					
$M_{\rm A}^{\rm CCQE}$	0.99 GeV	+25% -15%	-4.5%	-0.30	
$M_{\rm A}^{\rm CCRES}$	1.12 GeV	$\pm 20\%$	-3.9%	-0.20	
DIS CSMS	0.0	± 1.0	0.12	0.12	
Normalization:					
$A_{\rm eff}$ scale	+0%	[-90%,	-10%		
		+100%]			
Atmospheric muons:					
Atmospheric μ scale	+0%	$\pm 40\%$	-3.8%	-0.10	

nominal value that the fit starts at, a prior which can either be Gaussian with the given width or uniform, and the resulting best-fit value. For the parameters that have a Gaussian prior, the pulls (in units of σ) indicate how far the best-fit value is from the nominal value.

Appendix B: Results goodness of fit—The goodness of fit of the result is evaluated utilizing 1000 fits to pseudodata trials generated via Poisson fluctuating the expected events within the analysis bin given best-fit values of the resultant oscillation parameters. Figure 6 shows the expected and observed results for $\sin^2\theta_{23}$ and Δm_{32}^2



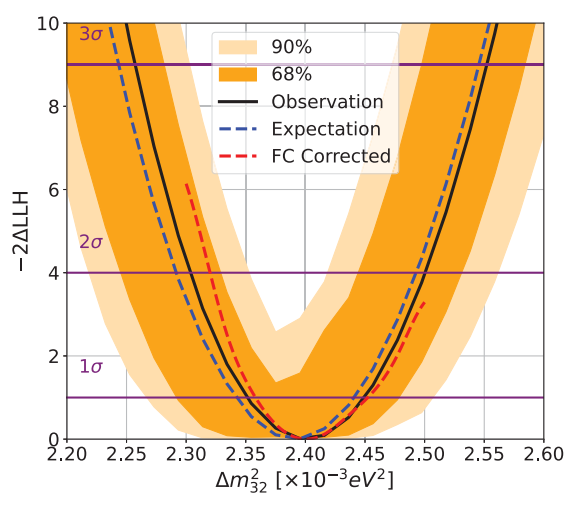


FIG. 6. Comparison of the observed (solid) results compared to the expectation (dashed blue) and the 68% and 90% distributions of 1000 pseudo-data trials (bands) produced at the best-fit point of the analysis for the atmospheric mixing angle (top) and mass splitting (bottom). The dashed red lines show the Feldman-Cousins [24] corrected contours.

overlaying the pseudo-data trials test statistic distribution. The observed contours are found to agree well with the anticipated 1σ fluctuations of the trials. Also shown are the Feldman-Cousins [24] corrected contours.